In the format provided by the authors and unedited.

Exciton resonance tuning of an atomically thin lens

Jorik van de Groep [1,4], Jung-Hwan Song [1], Umberto Celano [1,2], Qitong Li [1], Pieter G. Kik [1,3] and Mark L. Brongersma [1✉]

[1]Geballe Laboratory for Advanced Materials, Stanford University, Stanford, CA, USA. [2]IMEC Leuven, Leuven, Belgium. [3]CREOL, The College of Optics and Photonics, University of Central Florida, Orlando, FL, USA. [4]Present address: Van der Waals–Zeeman Institute for Experimental Physics, Institute of Physics, University of Amsterdam, Amsterdam, Netherlands. ✉e-mail: brongersma@stanford.edu

Supplemental Information for

Exciton-Resonance Tuning of an Atomically-thin Lens

Authors: Jorik van de Groep[1], Jung-Hwan Song[1], Umberto Celano[1,2], Qitong Li[1], Pieter G. Kik[1,3], and Mark L. Brongersma[1]*

Affiliations:

[1]Geballe Laboratory for Advanced Materials, Stanford University, Stanford, CA 94040, USA.

[2]IMEC Leuven, B-3001 Leuven, Belgium.
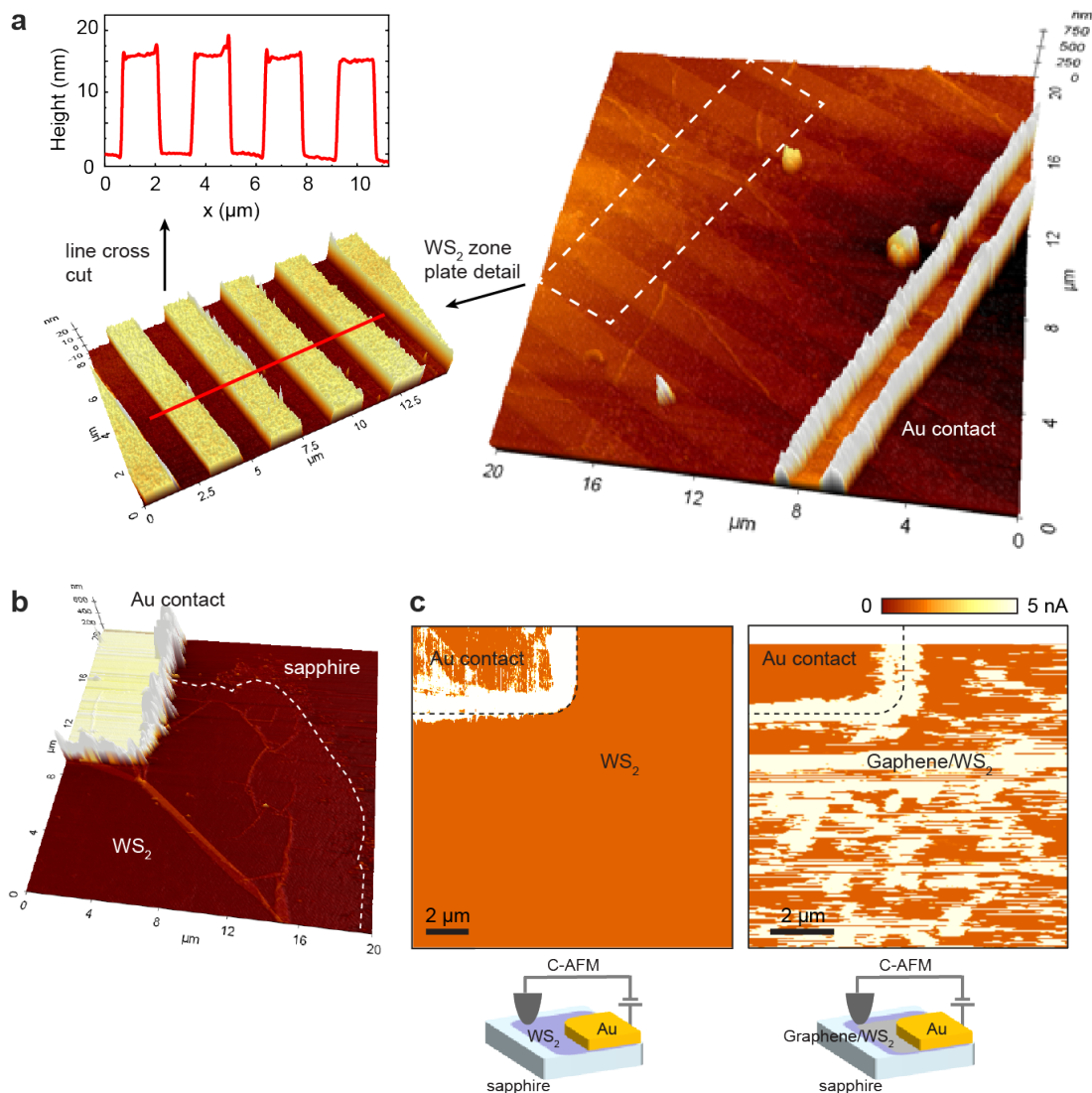
[3]CREOL, The College of Optics and Photonics, University of Central Florida, Orlando, FL 32816, USA.

*Correspondence to: brongersma@stanford.edu

This PDF file includes:

Supplemental Information Figures S1-S11
Supplemental Notes 1,2

Fig. S1 | Atomic Force Microscopy topography and surface conductivity characterization. a, 3D representation of the topological height measurements of a WS_2 zone plate (without graphene) and Au contact (right). The Au contacts are 100 nm high and have vertical extrusions at the edges due to non-perfect lift-off. A zoomed image and cross section of the zone plate pattern (left) show that the zone plate pattern was over-etched ~15 nm into the sapphire substrate. **b**, 3D representation of the topological height measurements on a WS_2 patch device on sapphire showing the patterning of the WS_2. **c**, Conductive-AFM measurements of the bare (left) and graphene-coated WS_2 (right) showing strongly enhanced surface conductivity in the presence of the graphene transparent electrode.
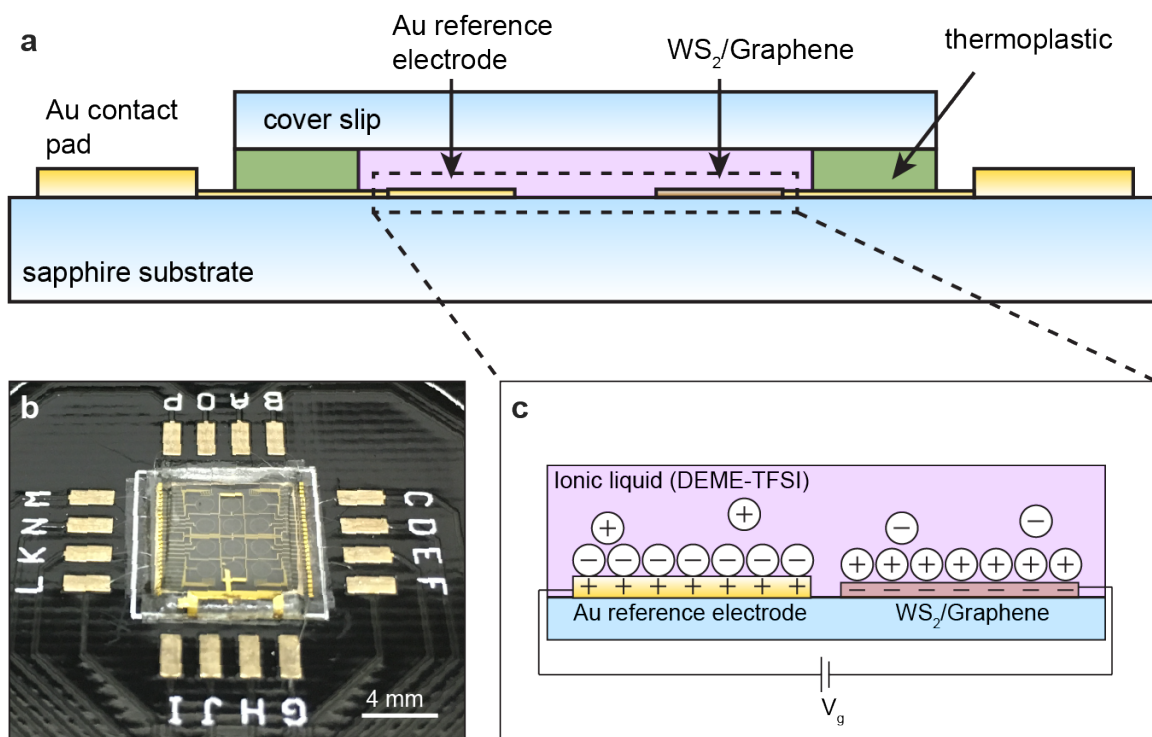
Fig. S2 | Electrochemical cell layout. a, Schematic cross section of the electrochemical cell fabricated on top of the sample, sealing the ionic liquid (DEME-TFSI) inside. **b**, Photograph of the $1{\times}1$ cm^2 sapphire substrate with 12 contacted zone plate lenses and completed electrochemical cell. The sample is mounted on a custom-made printed-circuit board to which the Au contact pads are wire-bonded. **c**, Zoomed image of the working principle of the ion-liquid gating. Charged molecules screen the Coulombic potential of the doped WS$_2$/Gr heterostructure and the Au reference pad.

1. Commercial WS$_2$ on sapphire

2. Large-area wet transfer monolayer graphene

3. Optical lithography for contacts

4. Ti/Au deposition + lift-off

5. EBL to cover device area

6. RIE to isolate device area and resist strip

7. EBL to define zone plate pattern

8. RIE to pattern WS$_2$/Graphene and resist strip

9. Build electrochemical cell (thermoplastic + cover glass)

10. Fill cell with ionic liquid (DEME-TFSI) and close ends with glue

Fig. S3 | Sample fabrication scheme. The numbers correspond to the steps described in the fabrication details in the Materials and Methods. EBL: electron-beam lithography; RIE: reactive-ion etching.
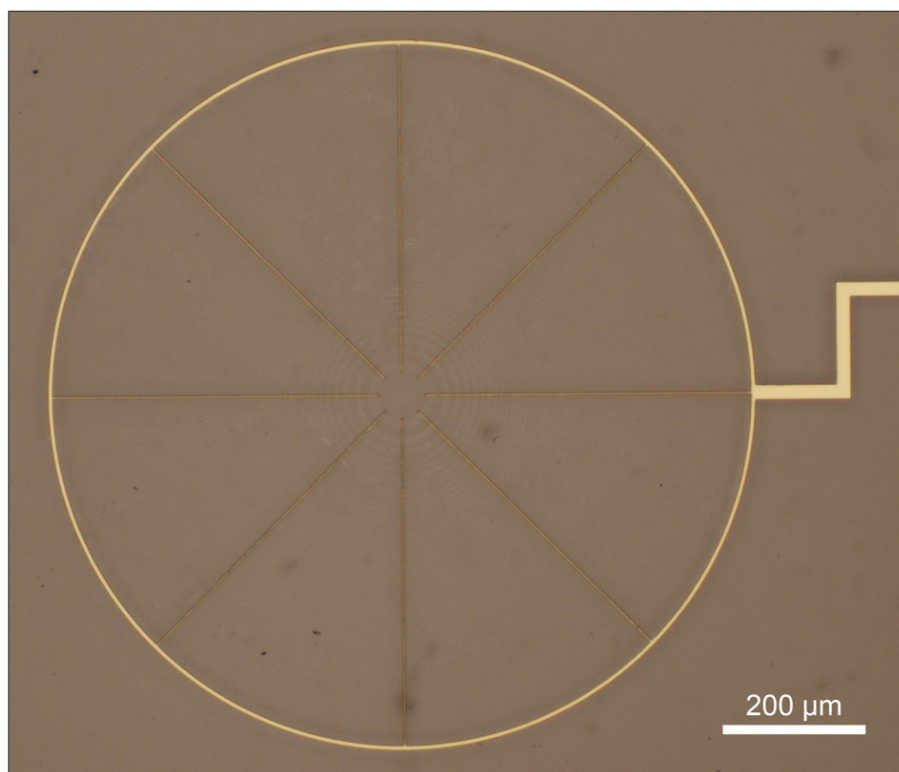
Fig. S4 | Large-area microscope image of contacted zone plate lens.
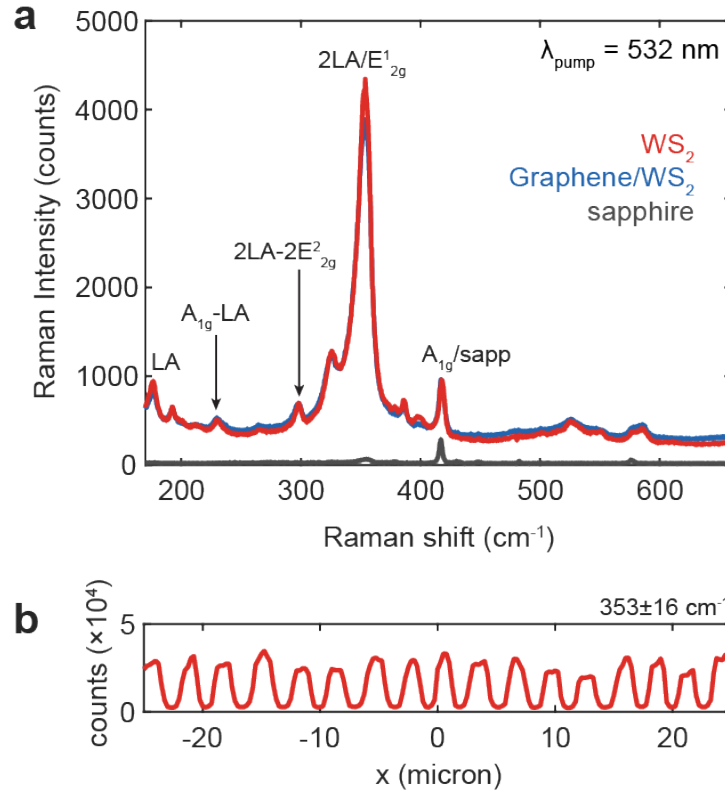
Fig. S5 | Raman material analysis. a, Raman spectra measured on bare WS_2 (red), WS_2/graphene heterostructure (blue), and bare sapphire substrate (grey). A_{1g} and E^1_{2g} are first order modes at the Brillouin zone centre, while LA are disorder-activated longitudinal acoustic phonons at the zone-edge[1]. **b**, Spatial line scan along part of the zone plate radius of the integrated main Raman peak intensity (353 ± 16 cm^{-1}), confirming the patterning of the WS_2.
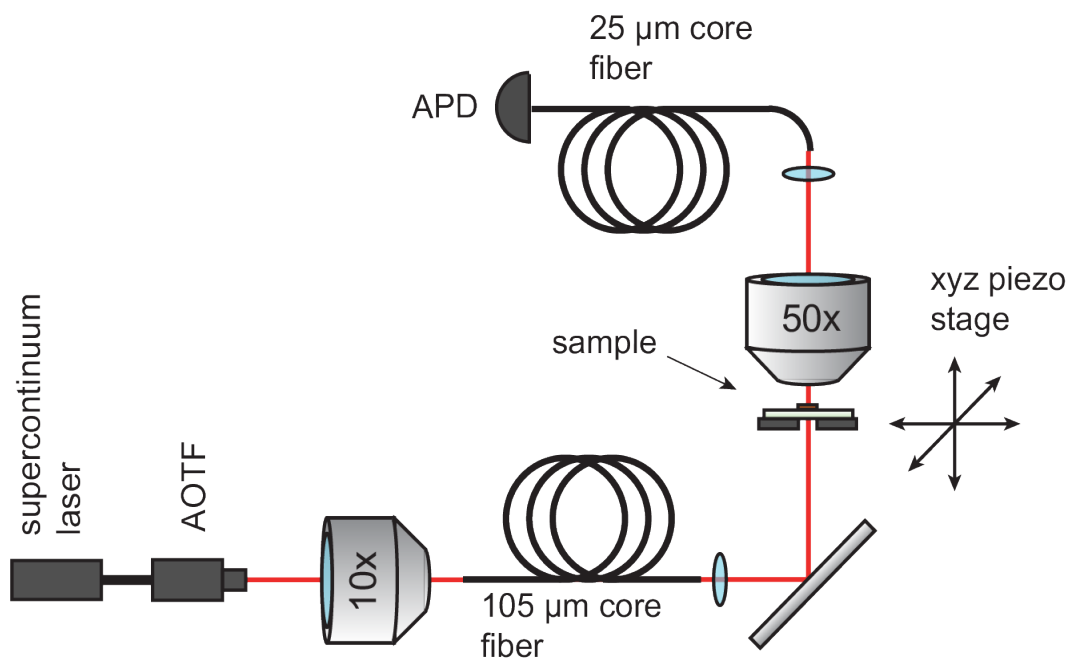
Fig. S6 | Schematic of confocal microscope setup used for focusing measurements. AOTF: acousto-optic tuneable filter, APD: avalanche photo diode.
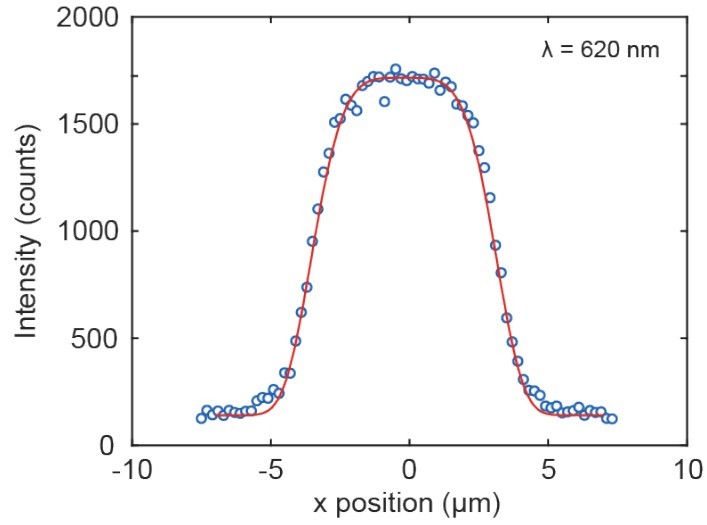
Fig. S7 | Cross section of 2D super-Gaussian fit to the focal spot. The spot size and shape are governed by the projection of the finite-sized multi-mode fibre core that is used to inject the laser light into the setup (see Fig. S6).

Fig. S8 | Non-resonant substrate contribution to focusing efficiency. The 15 nm over-etch into the sapphire substrate gives rise to a non-resonant background in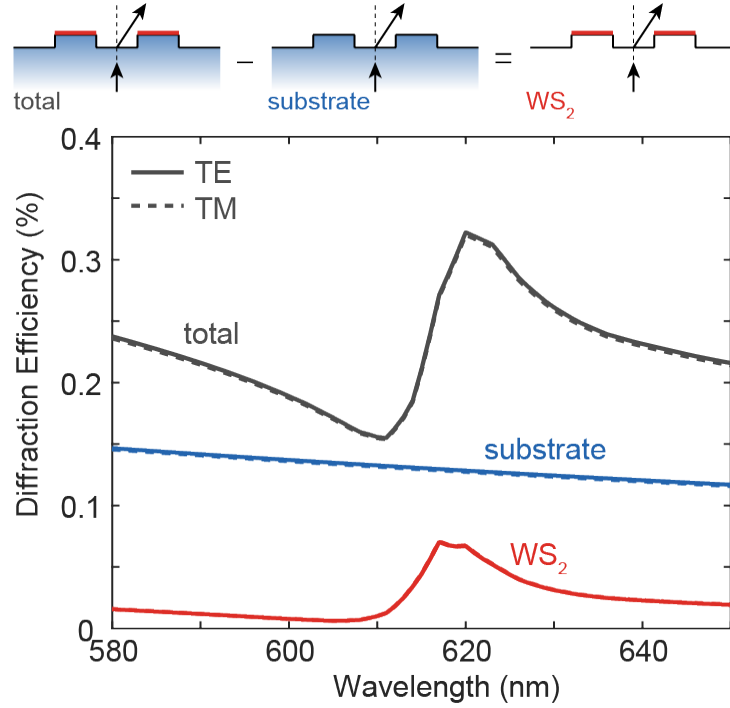 the focusing efficiency spectrum which limits the modulation depth. To study this, we perform a total-field scatter-field analysis of a diffractive grating that has dimensions analogous to the edge of the zone plate lens using rigorous-coupled wave-analysis (RCWA). The grating has a 2.6 µm period, a 50% duty cycle, and a 15 nm step height, with monolayer WS_2 on top of the ridges. The simulated diffraction efficiency (1st diffractive order in transmission) shows a clear asymmetric oscillation as a result of the WS_2 susceptibility (grey). By subtracting the complex field calculated for a bare substrate (no WS_2, blue), we obtain the scatter-field contribution of the WS_2 (red). Clearly, the non-resonant background diffraction contributes significantly and limits the modulation depth.
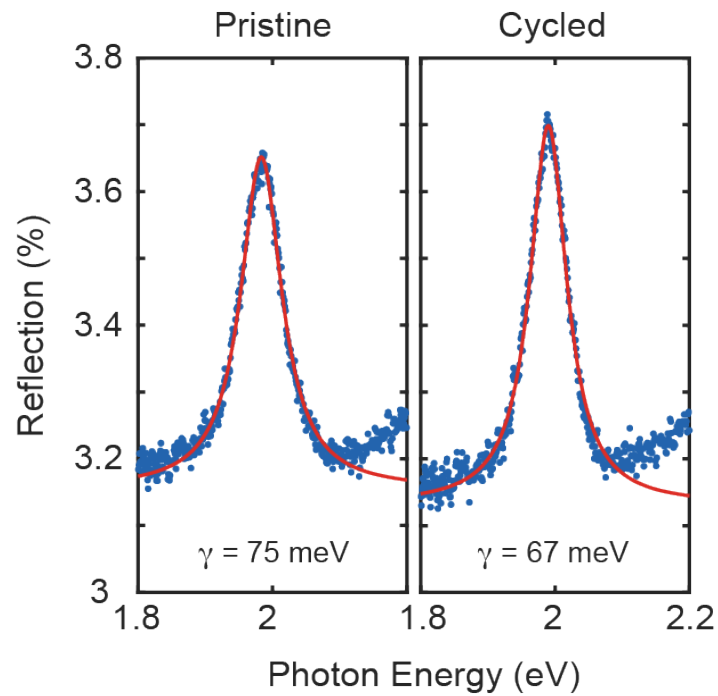
Fig. S9 | Excitonic line width narrowing in reflection spectrum upon first gating cycle. Reflection of WS$_2$ patch device measured inside electrochemical cell around A-exciton (blue) in pristine condition (left) and after the first cycle of ionic-liquid gating (right). A Lorentzian line shape is fitted to the data (red) and shows a 10% reduction in line width.

Supplemental Note 1: Analysis of potential optical efficiencies.

The theoretical efficiency of the atomically-thin zone plate lens can be calculated using conventional diffraction theory. To this end, we first use spectroscopic ellipsometry to experimentally measure the optical constants of our CVD-grown WS_2. The sample used is a monolayer of WS_2 on quartz, obtained from the same supplier (2dsemiconductors.com) as the WS_2 on sapphire used in our zone plate experiments. These optical constants are taken as representative for (low-quality) monolayer WS_2 in our efficiency analysis. Next, we use transfer-matrix calculations to retrieve the (complex) transmission coefficient of the sapphire/WS_2/air interface as well as the sapphire/air interface for the WS_2-covered and open rings of the zone plate, respectively. These complex transmission coefficients include both the amplitude and phase modulation by the monolayer WS_2 as the light propagates from within the sapphire substrate into the air superstrate. The effect of over-etching into the sapphire in the experiments is neglected. Then, we employ scalar Rayleigh-Sommerfeld diffraction theory[2] to calculate the intensity in the focus of the zone plate lens, using the same 1-mm diameter design as in our experiments. To calculate the zone plate focusing efficiency, we fit a Gaussian line shape to the focus, spatially integrate the intensity, and normalize to the power incident on the zone plate. The results are shown in red in Supplemental Fig. S10 and show good agreement with the experimental results.
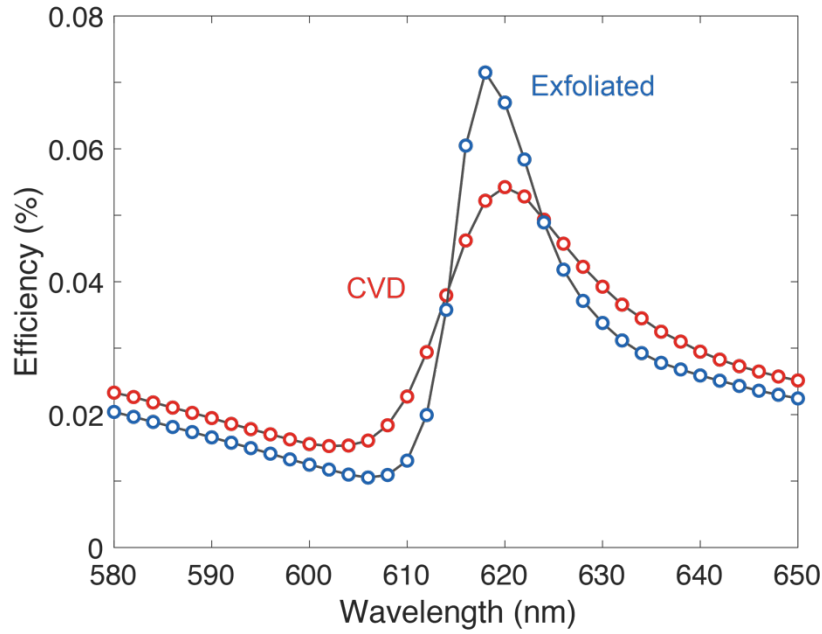
Fig. S10 | Calculated focusing efficiency for CVD-grown (red) and exfoliated (blue) WS₂ zone plate lens on sapphire.

To highlight the direct relation between the exciton line shape and focusing efficiency, we perform the same analysis using optical constants for exfoliated WS$_2$ (ref. [3]) which exhibits a higher materials quality and thereby stronger exciton resonance line shape. Indeed, the focusing efficiency shows a stronger peak and narrower line width as a result of improved material quality (blue in Supplemental Fig. S10).

Based on the insight that diffraction calculations give a valuable prediction of the optical diffraction efficiency, we perform a rigorous coupled-wave analysis (RCWA) to calculate the diffraction efficiency of a monolayer grating. The geometry is shown in Supplemental Fig. S11a. Light with $\lambda = 615$ nm is incident from the bottom quartz substrate and the grating period is 450 nm, which results in only four diffractive channels: the direct transmission (T_0), 0th order Light with $\lambda = 615$ nm is incident from the bottom quartz substrate and the grating period is 450 nm, which results in only four diffractive channels: the direct transmission (T_0), 0th order reflection (R_0), and the ±1 diffraction orders in reflection ($R_{\pm 1}$). We define the combined diffraction efficiency as the fraction of the total power that is redirected in the $R_{\pm 1}$ channels. We calculate this efficiency as a function of the complex susceptibility χ of the monolayer material, both for TE and

TM polarization (Supplemental Fig. S11b,c). TE polarization is defined as electric field parallel to the grating. Supplemental Fig. S11b,c show that for TM polarization diffraction efficiencies up to 40% can be achieved for susceptibilities $|\chi| \sim 4000$, while 10% efficiency is already achieved for $|\chi| \sim 350$. The oscillations for large real susceptibilities in Supplemental Fig. S11b are caused by geometrical optical resonances in the individual grating elements.
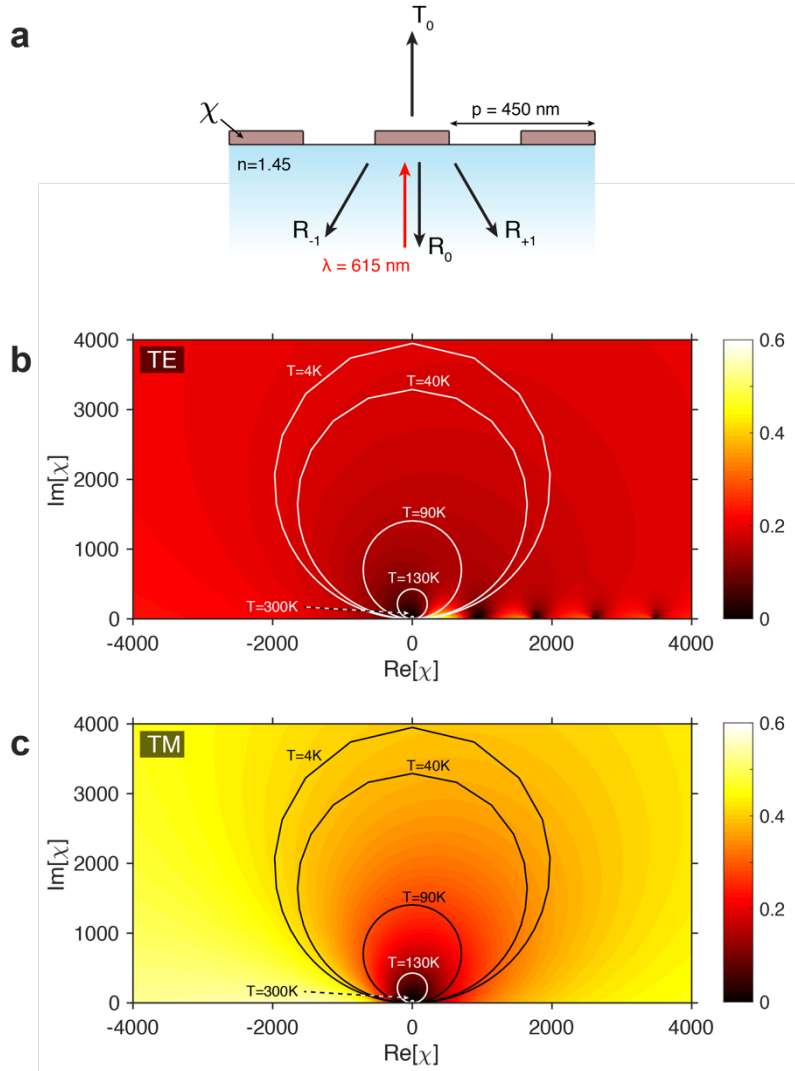
Fig. S11 | Diffraction efficiency analysis. a, Schematic of the geometry used for the diffraction efficiency analysis, as a function of the complex susceptibility χ of the monolayer grating (6.18 Å thickness). **b,c**, Calculated diffraction efficiency for TE (b) and TM (c) polarization. The exciton susceptibility for different temperatures is overlaid, as extracted from ref. [4].

To gain insight in the susceptibilities that can be achieved with exciton resonances at different temperatures, we extract the complex susceptibility of exciton resonances in a representative monolayer TMDCs from literature[4], and map these on the diffraction efficiency maps in Supplemental Fig. S11b,c. In short, we extract the absolute reflectance amplitude and line width for hBn-encapsulated monolayer $MoSe_2$ for different temperatures, and use the method described in ref. 4 to calculate the susceptibility from the monolayer reflectance. For high-quality TMDCs at low temperature, the optical response is dominated by the exciton resonance, and the non-zero background susceptibility becomes negligible[4]. High-diffraction efficiencies can be achieved in this case, as expected.

The response of our WS_2 material is also shown at room temperature at its exciton resonance around $\lambda = 615$ nm. The diffraction efficiency is low (<0.5% for T=300 K), in agreement with our experiments. From the literature, there is a clear path towards higher diffraction efficiencies at room temperature with 2D semiconductors. Because of the spatial confinement and reduced dielectric screening, these materials host room-temperature excitons that enhance light-matter interaction over the bulk. The actual strength of the interaction will ultimately depend on the materials quality, the bandstructure, the carrier density/distribution, the number of layers, and the environment. The rapid ongoing improvements in the growth, processing, and encapsulation of high-quality TMDCs can result in longer relaxation times by minimising impurity, defect, and surface roughness scattering. Ultimately, the scattering times will be limited by electron-electron and electron-phonon scattering. There is still a scarcity of the experimental values of the relaxation times in the literature and computational cost for calculating them are high. Improvements can thus logically be expected to emerge as more data becomes available. In terms of desired bandstructures, it is of importance to identify materials with a high joint density of optical states. Here, materials with nested band structures where the difference in the effective masses of the valence and conduction bands are minimised[5] or those exhibiting Van Hove singularities[6] are particularly promising to enhance light-matter interaction and 10% absorption/transmission modulation at room temperature seems achievable at room temperature given recent work[5]. Recently, novel Janus materials with structural anisotropy are also proving opportunities for strong light absorption/light transmission modulation (few percent per monolayer)[7]. Multi-layered stacks of 2D materials will naturally provide a strong optical response[5,8]. Stacked layers can already be

tuned electrochemically by ion intercalation[9,10] and other gating strategies are expected to become available as the processing of 2D materials improves. The optical response of 2D materials can also further be enhanced with the help of plasmonic or high-index Mie resonators. In these cases, one can leverage the light concentrating properties of the metallic and semiconductor nanostructures and the high electrical/optical tunability of the 2D materials. We present these arguments to show that there is significant room for improvements in many directions.

Supplemental Note 2: Applications of atomically-thin optical elements.

Besides the anticipated efficiency enhancements with improvements in material quality (Supplemental Note 1), we argue that highly-tuneable, but low-diffraction efficiency metasurfaces made from 2D materials have a different application space than high-efficiency, weakly-tuneable dielectric metasurfaces. We would like to emphasize that – even with their current performance – low-diffraction efficiency lenses can already be used in novel applications. These structures can be imperceptible to the human eye, offer high-tuneability at moderate voltages, and can produce focused beam spots with an intensity that easily exceeds the intensity of an incident light beam. As an example, for a 1 mm^2 lens, a 1 μm^2 focal spot, and a 0.1% diffraction efficiency the intensity in the focus is 1000 times higher than the incident beam. With these efficiencies, atomically-thin elements can already be used in novel heads-up displays for optical beam-tapping, flexible biosensing elements, and more. These optical techniques can provide valuable information about an optical scene (intensity, colour spectrum, polarization) or the user environment, without significantly perturbing the transmitted light beam. See e.g. recent work on beam-tapping[11], as well as transparent polarization- and colour-sensitive photodetection[12]. As an example of beam-tapping, ref. 11 demonstrates how a ~1% diffraction efficiency metasurface patterned in glass is used to redirect 1% of the light to a detection system placed in the arm of a pair of eyeglasses – without perturbing the user's view.

Given the very high dynamic contrast range of the eye (1000:1), atomically-thin optics on the surface of eyewear may also be used for direct retina projection in AR systems in conjunction with an appropriate projection system. For such systems, highly transparent optics is needed and very hard to create with metasurfaces constructed from strongly scattering plasmonic or Mie resonant

nanostructures. We argue that atomically-thin elements provide excellent opportunities for augmented and virtual reality applications. Realistically, it is (way) too early to evaluate the potential impact of this conceptually new technology. As the materials quality will increase over time, they may be able to take over/add to the functionality of conventional plasmonic and Mie-resonant metasurfaces.

References:

1. Berkdemir, A. *et al.* Identification of individual and few layers of WS_2 using Raman spectroscopy. *Sci. Rep.* **3**, 1755 (2013).

2. Marathay, A. S. & McCalmont, J. F. On the usual approximation used in the Rayleigh–Sommerfeld diffraction theory. *J. Opt. Soc. Am. A* **21**, 510 (2004).

3. Li, Y. *et al.* Measurement of the optical dielectric function of monolayer transition-metal dichalcogenides: MoS_2, $MoSe_2$, WS_2, and WSe_2. *Phys. Rev. B* **90**, 205422 (2014).

4. Scuri, G. *et al.* Large excitonic reflectivity of monolayer $MoSe_2$ encapsulated in hexagonal boron nitride. *Phys. Rev. Lett.* **120**, 37402 (2018).

5. Gupta, S., Shirodkar, S. N., Kutana, A. & Yakobson, B. I. In Pursuit of 2D Materials for Maximum Optical Response. *ACS Nano* **12**, 10880–10889 (2018).

6. Britnell, L. *et al.* Strong Light-Matter Interactions in Heterostructures of Atomically Thin Films. *Science* **340**, 1311–1315 (2013).

7. Yang, X., Singh, D., Xu, Z., Wang, Z. & Ahuja, R. An emerging Janus MoSeTe material for potential applications in optoelectronic devices. *J. Mater. Chem. C* **7**, 12312–12320 (2019).

8. Papadakis, G. T. *et al.* Ultralight Angstrom-Scale Optimal Optical Reflectors. *ACS Photonics* **5**, 384–389 (2018).

9. Gong, Y. *et al.* Spatially controlled doping of two-dimensional SnS_2 through intercalation for electronics. *Nat. Nanotechnol.* **13**, 294–299 (2018).

10. Xiong, F. *et al.* Li Intercalation in MoS_2: In Situ Observation of Its Dynamics and Tuning Optical and Electrical Properties. *Nano Lett.* **15**, 6777–6784 (2015).

11. Li, Q.T. *et al.* Free-space optical beam tapping with an all-silica metasurface. *ACS Photonics* **4**, 2544–2549 (2017).

12. Li, Q.T., van de Groep, J., Wang, Y., Kik, P. G. & Brongersma, M. L. Transparent multispectral photodetectors mimicking the human visual system. *Nat. Commun.* **10**, 4982 (2019).